University of Montana

ScholarWorks at University of Montana

Physics and Astronomy Faculty Publications

Physics and Astronomy

12-14-2014

Spectral Evolution of Energetic Neutral Atom Emissions at the Heliospheric Poles as Measured by *IBEX* during its First Three Yeras

M. Dayeh
Southwest Research Institute

F. Allegrini
Southwest Research Institute; University of Texas - San Antonio

R. DeMajistre
Johns Hopkins University

M. I. Desai
Southwest Research Institute; University of Texas - San Antonio

R. W. Ebert
Southwest Research Institute

Follow this and additional works at: https://scholarworks.umt.edu/physics_pubs
See next page for additional authors
Part of the The Sun and the Solar System Commons

Let us know how access to this document benefits you.

Recommended Citation

Authors

M. Dayeh, F. Allegrini, R. DeMajistre, M. I. Desai, R. W. Ebert, S. A. Fuselier, Paul H. Janzen, G. Livadiotis, D. J. McComas, Daniel B. Reisenfeld, N. A. Schwadron, and M. Siewert

SPECTRAL EVOLUTION OF ENERGETIC NEUTRAL ATOM EMISSIONS AT THE HELIOSPHERIC POLES AS MEASURED BY *IBEX* DURING ITS FIRST THREE YEARS

M. A. Dayeh[1], F. Allegrini[1,2], R. DeMajistre[3], M. I. Desai[1,2], R. W. Ebert[1], S. A. Fuselier[1], P. Janzen[4],
G. Livadiotis[1], D. J. McComas[1,2], D. Reisenfeld[4], N. A. Schwadron[1,5], and M. Siewert[6]

[1] Southwest Research Institute, San Antonio, TX 78228, USA; maldayeh@swri.edu
[2] University of Texas at San Antonio, San Antonio, TX 78249, USA
[3] Johns Hopkins University Applied Physics Laboratory, Laurel, MD 20723, USA
[4] University of Montana, Missoula, MT 59812, USA
[5] University of New Hampshire, Durham, NH 03824, USA
[6] Institut für Astronomie der Universität Bonn, Abteilung f. Astrophysik und Extraterrestrische Forschung, Auf dem Hügel 71, D-53121 Bonn, Germany

ABSTRACT

The *Interstellar Boundary Explorer* (*IBEX*) mission continues to measure energetic neutral atom (ENA) emissions produced by charge exchange between solar wind (SW) protons and interstellar neutrals at the edge of our heliosphere. Using the first 3 yr of *IBEX-Hi* ENA measurements (2009–2011), we examined the spectral evolution of ∼0.5–6 keV ENAs at the polar regions (above 60°). We found the following: (1) pixels with a characteristic "ankle" spectra (lower spectral index at higher energies) increase by ∼5% in 2010 and ∼10% in 2011 compared to 2009. (2) The averaged spectral index in 2011 is smaller than that of 2009. (3) The slope of the ENA spectrum above ∼1.7 keV is more variable than the slope below ∼1.7 keV. The lower spectral index at higher energies of the spectrum does not appear to be caused by an increase of the ENA production at these energies, but rather from a consistent decrease at lower energies. (4) The decrease in polar ENA fluxes does not correlate significantly with the averaged SW dynamic pressure, back-traced in time to 1 AU along the flow streamlines (originating between 10° and 30° for slow SW, and 60° and 80° for fast SW), assuming these are the respective conditions of ENA progenitors back in time. These results provide insights into the complexity of relating the slow and fast SW contributions to polar ENAs and shed light on how the solar output and the resulting change in the global heliospheric structure possibly affect the heliosheath (HS) populations.

Key words: solar wind – Sun: heliosphere

Online-only material: color figures

1. INTRODUCTION

The *Interstellar Boundary Explorer* (*IBEX*) mission (McComas et al. 2009) continues to provide energy-resolved all-sky maps of energetic neutral atoms (ENAs) imaging the interaction region between the heliospheric boundary and the interstellar medium. *IBEX* has two single-pixel ENA cameras, *IBEX-Hi* (Funsten et al. 2009a) and *IBEX-Lo* (Fuselier et al. 2009) covering an overlapping energy range between ∼0.01 keV and ∼6 keV. Since its launch in 2008 October, *IBEX* has provided several unprecedented discoveries of the heliospheric interface interactions, the most notable being the discovery of a ribbon of enhanced ENA emissions comprising an almost circular (∼300°) and narrow (∼20°) arc that is apparently centered on the direction of the interstellar magnetic field, draped around the heliosphere (e.g., Funsten et al. 2013).

To date, numerous studies on *IBEX* global ENA emissions—created in the heliosheath (HS) via charge exchange processes—have shown that they exhibit temporal changes at different energies and appear to correlate with variations of the solar wind (SW) latitudinal structure originating at the Sun (McComas et al. 2012b; Schwadron et al. 2011; Dayeh et al. 2011; Funsten et al. 2009b). In a detailed study, Dayeh et al. (2011) showed that different regions in the sky are characterized by distinct spectral shapes (see also Funsten et al. 2009b); in particular, single power laws dominate at mid- and low latitudes outside the ribbon, knee-like broken spectra (i.e., the spectrum steepens with increasing energy) dominates across the ribbon, and ankle-like broken spectra exists at the poles (i.e., the spectrum flattens

with increasing energy). These studies showed that the spectral shapes of ENAs are strongly correlated (up to ∼6°) with latitudinal variations of the SW speed structure (McComas et al. 1998, 2008) obtained a few years earlier by *Ulysses*/SWOOPS (Bame et al. 1992) in the inner heliosphere inside ∼5 AU.

Schwadron et al. (2011) showed that ENAs in the *IBEX* ribbon are characterized by a knee-like broken spectrum with a break point that moves with latitude. These results indicate that even though the processes of generating the ribbon and the globally distributed ENA fluxes could be different, the SW still has a strong imprint on the ordering of ENA spectral structure at different latitudes. McComas et al. (2013) illustrated this ENA ribbon ordering by the SW at different latitudes. They showed low-energy ENA enhancements at low latitudes likely originating along the ecliptic from the shocked slow SW population and high-energy ENA enhancements at high latitudes possibly originating from the fast SW component.

Variations of polar ENA emissions have also been studied. Taking advantage of *IBEX*'s spinning and orbit configuration, which maximizes polar viewing, Reisenfeld et al. (2012) examined ENA fluxes in individual orbits from the polar directions over the *IBEX-Hi* energy range during a 2 yr period. They found that there is an energy-dependent decrease in ENA fluxes varying from no drop at 0.71 keV up to 70% at 1.1 keV. At higher energies, the decrease ranged between 10% and 50%. The authors correlated this decreasing trend with the steady decline in SW dynamic pressure observed at 1 AU between 2005 and 2009, the likely period when SW protons that provide the source for ENAs observed by *IBEX* would have been outbound from the
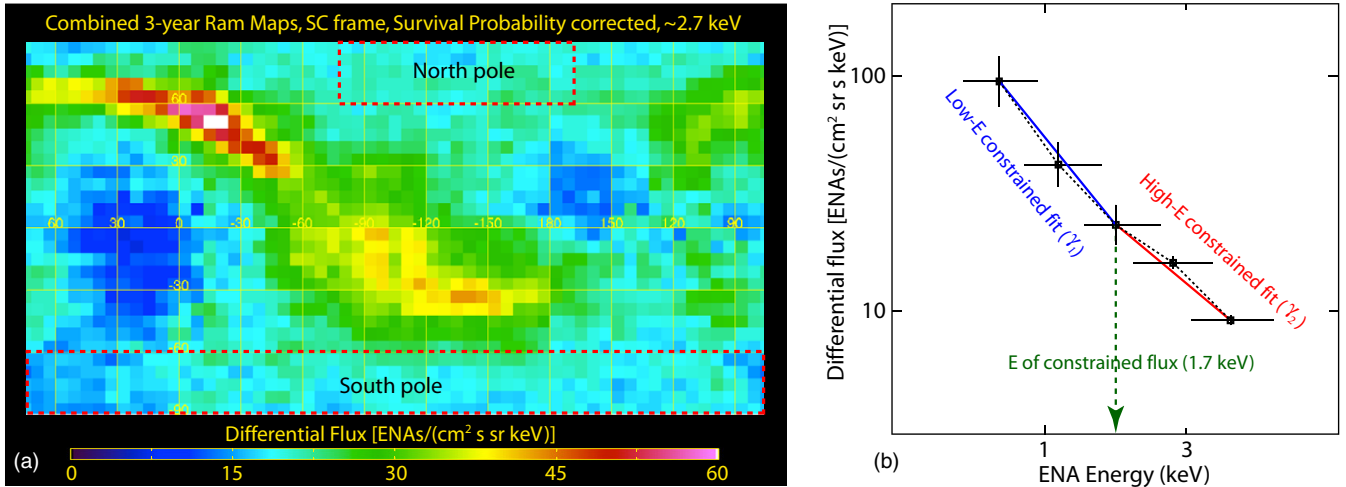
Figure 1. (a) Three-year, exposure-averaged all-sky map of ENA fluxes (orbits 11 through 56) at ∼2.7 keV as measured in the frame of the *IBEX* spacecraft in the ram direction. Dashed red lines mark the boundaries of north and south polar regions used throughout the analysis. (b) An illustration of fitting two single power laws to the ENA spectrum. Fits are constrained at the mid-energy (∼1.7 keV); see the text for details.

(A color version of this figure is available in the online journal.)

Sun. Moreover, Allegrini et al. (2012) examined the polar ENA spectra by accounting for the time dispersion effects, assuming a fixed ENA source for all energies. These authors found that the spectral shape at the poles exhibits a statistically significant change with time. In a recent study, Dayeh et al. (2012) showed evidence that the ankle-like broken spectrum at high latitudes is due to the coexistence of two progenitor ion populations in the slow and fast SW at the polar regions. The coexistance of these two populations arises naturally from the deflection of the interplanetary magnetic field lines due to the heliospheric flow and the solar rotation, creating a spiral that carries the slow SW component from low latitudes to high latitudes (see also Livadiotis et al. 2011, 2012; Siewert et al. 2014).

IBEX provides one sky map every six months. Recently, McComas et al. (2012a) provided an updated and validated data set of six six-month maps from the first 3 yr (2008 December–2011 December) of *IBEX* ENA observations. These data included corrections for the time-variable cosmic-ray background as well as the orbit-by-orbit variations in the survival probability for ENAs reaching 1 AU from the outer heliosphere. Using the validated data over the 3 yr period, the authors quantified a dimming trend in global ENA emissions. The amount of dimming differs for different energies and varies for different look directions in the sky. In addition, combined maps and enhanced statistics revealed new features in the heliospheric structure. For instance, using the combined 3 yr data, McComas et al. (2013) examined the downwind region of the heliosphere for the first time and identified a broad slow SW plasma sheet crossing with fast wind tail regions to the north and south. The slow wind plasma sheet exhibits the steepest ENA spectra in the sky and appears as a two-lobed structure (named *Port* and *Starboard*, in the context of the heliospheric cocoon motion through interstellar space) that is twisted in the alignment direction of the interstellar magnetic field.

In this paper, we use the 2009–2011 validated *IBEX* observations to examine the spectral variations at low (0.7–1.7 keV) and high (1.7–4.3 keV) energies across the *IBEX-Hi* energy range and discuss the implications of their possible sources originating in the SW. In particular, we found that ENA fluxes at different energies decrease at different rates over the 3 yr period (2009–2011). This decrease in ENA flux results in spectral

flattening of ENAs at energies above ∼1.7 keV that does not seem to correlate with the dynamic pressure drop of their SW respective progenitors backtracked in time. These results provide insights into the complexity of slow and fast SW distributions in the HS and how they contribute to polar ENAs, highlighting the need for more modeling efforts to better understand the observed ENA variations.

2. OBSERVATIONS

Data used in this paper are obtained from the first validated 3 yr (2009–2011) release of *IBEX* ENA observations.[7] ENA data have been corrected for the time-variable cosmic-ray background and for variations in the survival probability for ENAs reaching 1 AU from the outer heliosphere. A detailed description of the data set can be found in McComas et al. (2012a).

Throughout the analysis, we use the RAM data where observation times are those when the spacecraft rams into the ENA flow, resulting in better statistics. Since we are investigating relative variations of fluxes over time, correction for the Compton–Getting (CG) effect resulting from the spacecraft motion is not required in this case. We note that the CG effect maximizes along the flow velocity vector and decreases as the cosine with latitude until it vanishes at the poles. For our case, the uncertainty due to this effect does not exceed a maximum of ∼5% at 72° (latitude) at ∼0.7 keV. For both south and north polar caps, we examine latitudes above 60°, which is the approximate limit of ENA polar regions determined by McComas et al. (2010), and is also the region where the SW flow is mostly fast (>600 km s⁻¹; e.g., McComas et al. 2008). ENA contributions from the *IBEX* ribbon at high latitudes make it difficult to separate them from the globally distributed ENA fluxes, especially that the origin of these two populations may be different (McComas et al. 2011). We thus exclude all pixels where these ribbon enhancements appear to overlap with the globally distributed ENA fluxes above 60°, assuming an almost circular ribbon (Funsten et al. 2013). This leaves us with a north polar region bounded between −78° and 132° in longitude, as indicated by the dashed red lines in Figure 1(a). This figure is

---
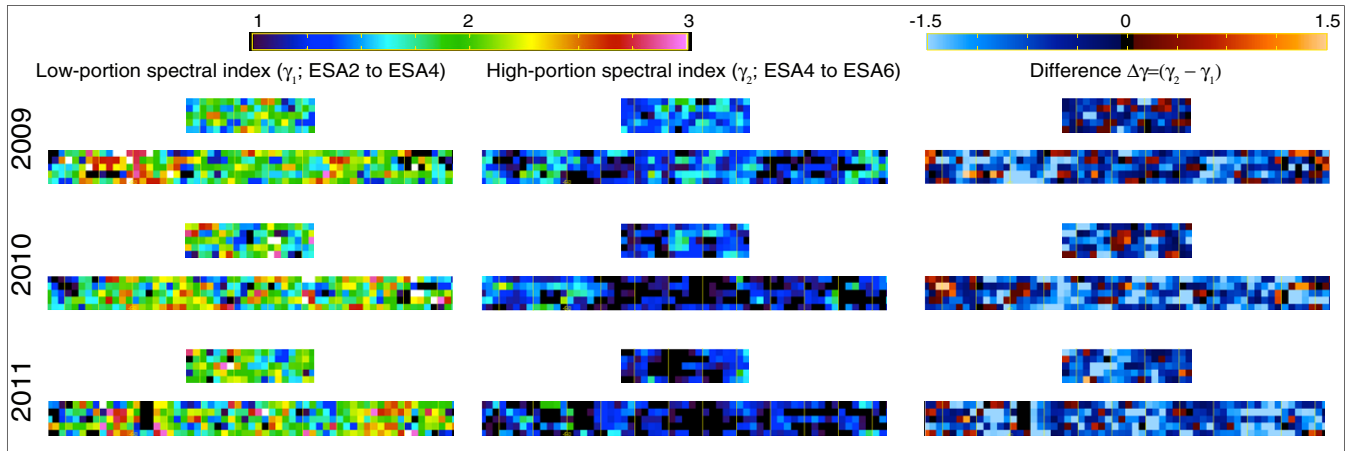
Figure 2. Spectral maps of the south and north poles at (a) low and (b) high energies for the 3 yr of this study. (c) Difference between panels (a) and (b).
(A color version of this figure is available in the online journal.)

Table 1
Percentage Changes in the Three Possible Values of $\Delta\gamma$ over 3 yr in Both Poles

Energy Channel (keV)	Percentage Change in ENA Fluxes from 2009 to 2011 (North Pole)	Percentage Change in ENA Fluxes from 2009 to 2011 (South Pole)
~0.7	~9.8	~4.5
~1.1	~27.2	~24.7
~1.7	~25.0	~17.5
~2.7	~6.8	~8.0
~4.3	~7.9	~2.9

the combined, exposure-averaged, ENA sky map over the 3 yr at ~2.7 keV and in the RAM direction. Note that interesting features appear in the 3 yr combined maps that were not previously clear in the individual six six-month maps. Most notably, the heliotail region that extends ~180° in longitude centered on the downwind direction and comprises two with significantly lower ENA emissions at energies above ~2.7 keV (see McComas et al. 2013).

Numerous studies have shown that the polar ENA spectra comprise two distinct slopes at lower and higher energies with a characteristic break around ~1.7 keV. To examine the polar variations of ENAs, we adopt the technique used by Dayeh et al. (2011) in which the ENA spectrum is divided into two portions, each is described by a power law of the form $j = j_0 E^{-\gamma}$ (where j is the ENA flux, E is the energy, and γ is the spectral index). This gives rise to a low-energy portion (characterized by spectral index γ_1) and high-energy portion (characterized by spectral index γ_2); the fit is constrained at the mid-energy point of ~1.7 keV, which then works as a pivot between both portions of the spectrum. Figure 1(b) illustrates this approach. The difference between the high- and low-energy portions of the spectral indices represents the quantity $\Delta\gamma = \gamma_2 - \gamma_1$, which has three possible values: (1) positive, meaning the spectrum is steeper at higher energies (or flatter at lower energies); (2) zero or close to zero (within 1σ), meaning the spectrum can be described by a single power law; and (3) negative, meaning the spectrum gets flatter at high energies (or steeper at lower energies). Here, we note that we have quantified the effect of the intrinsic variability of the flux at ~1.7 keV on the results and found that it affects the errors of the fitted slopes γ_1 and γ_2 by only ~15%.

Using the yearly RAM maps of 2009–2011, we applied the spectral fitting technique described above to every pixel in the selected polar regions. Figure 2 shows the spectral indices in both poles for the low (panel (a); spectral indices γ_1) and the

high (panel (b); spectral indices γ_2) energy fits, respectively. Panel (c) shows the difference of the spectral indices $\Delta\gamma = \gamma_2 - \gamma_1$ for each year. $\Delta\gamma$ indicates the spectral behavior over the 3 yr of observations. Red indicates a knee-shaped spectrum that steepens at higher energies, and blue indicates an ankle-shaped spectrum that flattens at higher energies. The darker the color (approaching zero), the closer the ENA spectrum in that pixel is to be described by a single power law.

While no clear variations can be seen in the low-energy spectral fits over the 3 yr period (panel (a)), consistent and significant changes appear in the high-energy portion of polar ENA spectra (panel (b)) with a clear darkening over time and at all longitudes. This darkening indicates a flattening of the spectral index. It is important to note that the lack of spectral variations in the low-energy portion (panel (a)) does not mean that fluxes are not changing since a consistent drop of the flux at all energies maintains a fixed spectral index. To better illustrate the reason for this spectral behavior, we plot in Figures 3(a) and (b) the annual averaged spectra of all pixels in both polar regions, normalized to the "pivot" energy point (~1.7 keV). Percentage variations of annual fluxes at all energies are listed in Table 1.

This figure shows that the low-energy portion maintains an almost constant slope, while the higher-energy portion of the spectrum flattens at different rates. Interestingly, the largest ENA drop takes place at ~1.1 keV, which is within our defined low-energy range. Figures 3(c) and (d) show the histogram of spectral indices in both poles' pixels over the 3 yr. Clearly, while almost no change can be seen for γ_1, the entire distribution of γ_2 shifts to the left, indicating an overall spectral flattening. Here, we note that the width of the distribution reflects the variability of the spectral index of all pixels in the polar regions and will not be interpreted as an error of the spectral index in individual pixels.
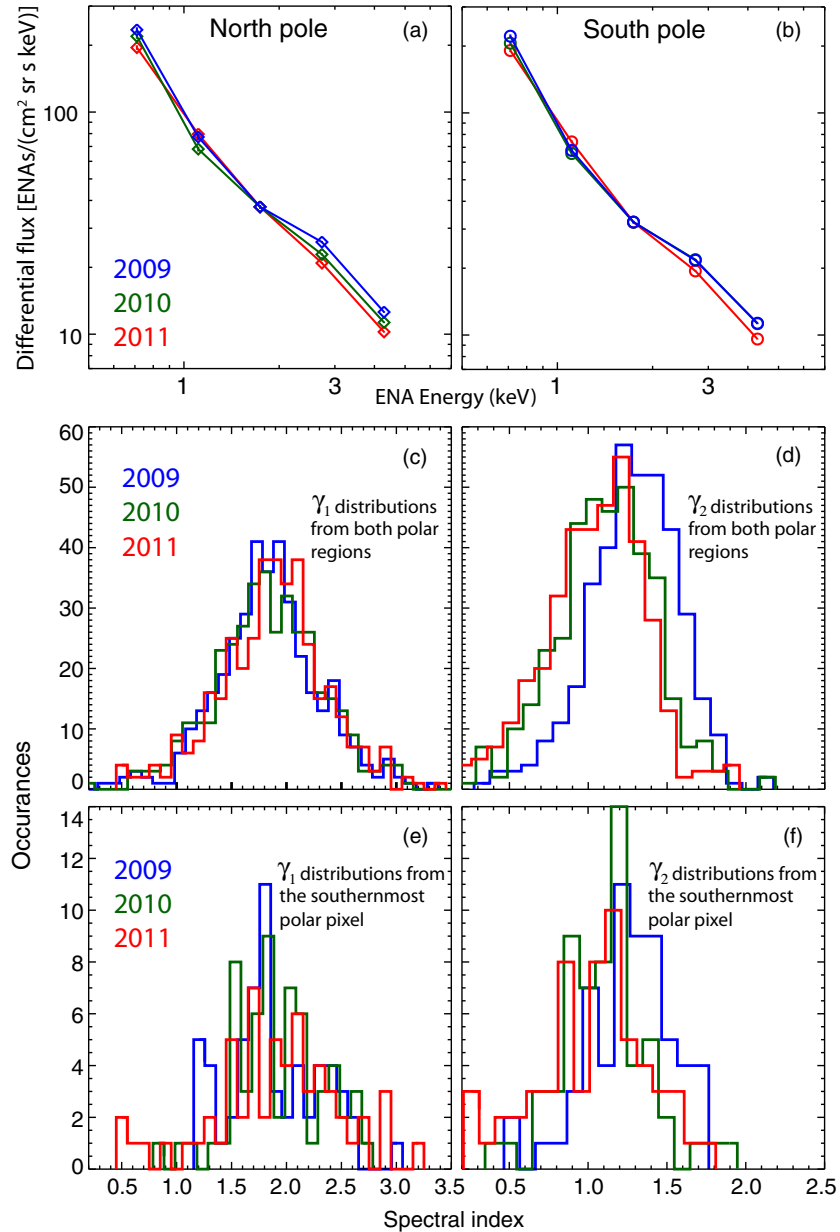
Figure 3. ((a) and (b)) Averaged spectra at both poles normalized to ∼1.7 keV, as measured in the spacecraft frame; see Table 1 for the details. ((c) and (d)) Distribution of the spectral indices at low (γ_1) and high (γ_2) energies over the 3 yr period studied here. Each histogram includes pixels from both poles. ((e) and (f)) Similar to panels (c) and (d), but for the southernmost polar pixel. These latter panels highlight the intrinsic variability of ENA spectra at the continuously observed polar pixels.

(A color version of this figure is available in the online journal.)

To verify the latter claim, we plot in Figures 3(e) and (f) the distributions of the spectral indices (in the polar region, a characteristic break around ∼2.7 keV)(γ_1 and γ_2) at the south-ernmost polar pixel as measured annually over three different years. Here, each distribution contains data acquired from all orbits over a full year, since IBEX continuously observes the poles as it spins. To examine the polar variatioserves the poles as it spins. These panels show that the distribution of indices at the exact polar pixel (south pole in this case) varies by the same order as those of the polar regions shown in Figures 3(c) and (d). These results shed light on the complexity of how dynamic polar ENA sources possibly are. In addition, this highlights the large variability of the spectral index over multiple measure-ments of the same polar pixel, which needs to be considered when interpreting ENA spectral results, at least from the poles. Note that these distributions representing a single pixel (panels

3(e) and (f)) can only be examined at the poles since they are continuously viewed by *IBEX* while at the equator; for instance, only one measurement pixel is acquired every six months, and its spectra lie within these representative distributions.

To further understand these changes, we show in Figure 4 all $\Delta\gamma$ values (from Figure 2(c)) of south and north polar pixels normalized to the propagated error, $\sigma_{\Delta\gamma} = \sqrt{\gamma_1^2 + \gamma_2^2}$, and plotted against the mid-energy flux at which the fitted spectrum was constrained (∼1.7 keV). Here, positive values of $\Delta\gamma$ (red) indicate spectra that steepen at higher energies, and negative values (in blue) indicate spectra that flatten at higher energies. Values where $\Delta\gamma$ is within 1σ of the propagated error are considered within the zero range and thus can be fitted by a single power law (shown in green). We note that the same exact pixels are studied over the 3 yr and missing pixels in any of the maps are omitted from the other two maps.
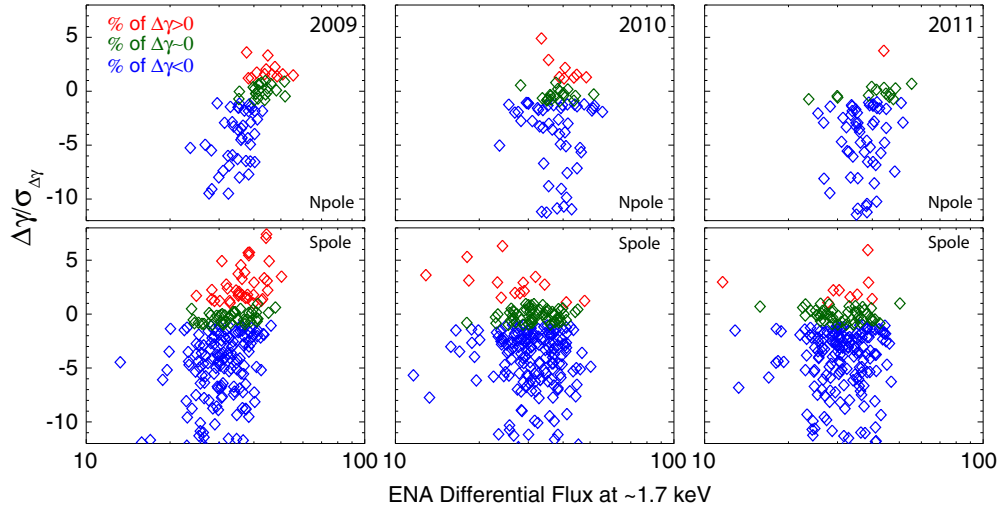
Figure 4. Normalized $\Delta\gamma$ values for pixels in the (a) north and (b) south polar regions plotted vs. ENA flux at ~1.7 keV. Red indicates $\Delta\gamma > 0$, blue indicates $\Delta\gamma \lesssim 0$, and green shows values bounded by $-1\sigma < \Delta\gamma < +1\sigma$.

(A color version of this figure is available in the online journal.)

Table 2
Percentage Changes in the Three Possible Values of $\Delta\gamma$ over 3 yr in Both Poles

Year	North Pole Pixels ($N = 95$)			South Pole Pixels ($N = 290$)		
	Percent of N_- ($\Delta\gamma < 0$)	Percent of N_0 ($\Delta\gamma \sim 0$)	Percent of N_+ ($\Delta\gamma > 0$)	Percent of N_- ($\Delta\gamma < 0$)	Percent of N_0 ($\Delta\gamma \sim 0$)	Percent of N_+ ($\Delta\gamma > 0$)
2009	61.4	23.9	14.8	71.7	15.0	13.3
2010	69.3	21.6	9.1	73.1	21.0	5.9
2011	84.1	18.8	1.1	79.0	17.1	3.8

Table 2 summarizes the statistical details of the data shown in Figure 4. As indicated, the percentage of pixels with positive $\Delta\gamma$ decreases consistently with time at both poles; at the same time, the percentage of pixels with negative $\Delta\gamma$ increases and at a similar rate. Pixels fluctuating around $\Delta\gamma \sim 0$ remain almost constant.

2.1. Are These Changes Statistically Significant?

In order to examine whether the observed changes reflect a real variation pattern, we performed a statistical significance test. First, we estimate the errors of the numbers of positive N_+ ($\Delta\gamma > 0$), negative N_- ($\Delta\gamma < 0$), and zero N_0 ($|\Delta\gamma| \leqslant \sigma_{\Delta\gamma}$) events. Then, we comprise extensive random permutations of all three possible outcomes of $\Delta\gamma$, where $\Delta\gamma_{\text{new}} = \Delta\gamma + \sigma_{\Delta\gamma} \cdot \varepsilon$. We use uniformly distributed random numbers ε between -1 and 1 (Figure 5(a)), one for each polar region pixel (385 in total for both poles, $\{\varepsilon_j^k\}_{j=1}^{385}$) and one set for each year, $\{\varepsilon_j^k\}_{j=1}^{385}$, $k = 1, 2, 3$, to randomly imitate the three $\Delta\gamma$ outcomes N_+, N_-, N_0. By repeating the process t times, we obtain t values of the triplet, $\{(N_+)_i, (N_-)_i, (N_0)_i\}_{i=1}^t$, and thus we can estimate their mean values and variance. We calculate the correlation coefficient between any two sets of random numbers, $\{\varepsilon_{ij}\}_{j=1}^{385}$, $i = 1, 2, t$; there are $t(t-1)/2$ combinations after the passage of t iterations. As expected, the coefficients are close to zero so that the utilized sets of random numbers to different iterations are uncorrelated with each other. This is shown in Figure 5(b), where we observe that the correlation coefficients are normally distributed with a Gaussian distribution N (mean $= 0$, standard deviation $= 0.05$) fitting the histogram of the coefficients. The statistical convergence of the mean and variance of the triplet $N_+, N_-,$

Table 3
Results of the Statistical Significance Test

| Test of Constancy for:	N_+	N_-	N_0
Mean and Variance, $\bar{p} \pm \delta\bar{p}$	12 ± 5	80 ± 6	7.3 ± 1.0
$\chi_{\text{est}}^2 = \chi^2(\bar{p})$	69	12.4	0.90
$\chi_{\text{red}}^2 = \frac{1}{N-1}\chi_{\text{est}}^2$	35.5	2.48	0.45
p-value	$\ll 0.05$	$\ll 0.05$	0.36 (>0.05)
Test rate	Highly unlikely	Highly unlikely	Highly likely

N_0 is shown in Figure 5(c), where the iterations are taken up to $t \sim 10^5$.

Having estimated the values of $\langle N_+ \rangle \pm \sigma_{N+}$, $\langle N_- \rangle \pm \sigma_{N-}$, $\langle N_0 \rangle \pm \sigma_{N0}$, we test the statistical hypothesis of the constancy of these values. The results are shown in Table 3. Here, a p-value (e.g., Livadiotis 2007, 2014) smaller than the significance level of ~0.05 typically means an unlikely occurrence of the hypothesized change.

The statistical tests are rejected for the positive and negative events, while the test for the zero events is accepted. The analysis strongly suggests that the positive events are decreasing and the negative events are increasing within the examined 3 yr. The zero events are highly likely to be constant.

3. DISCUSSION

We studied the spectral evolution of polar ENA emissions during 3 yr of continuous observations by *IBEX-Hi* over energy ranges ~0.7–1.7 keV (spectral index γ_1) and ~1.7–4.3 keV (spectral index γ_2), respectively. In particular, we calculated the difference of the spectral indices at both energy ranges ($\Delta\gamma = \gamma_2 - \gamma_1$) and examined the evolution of $\Delta\gamma$ during this period. We
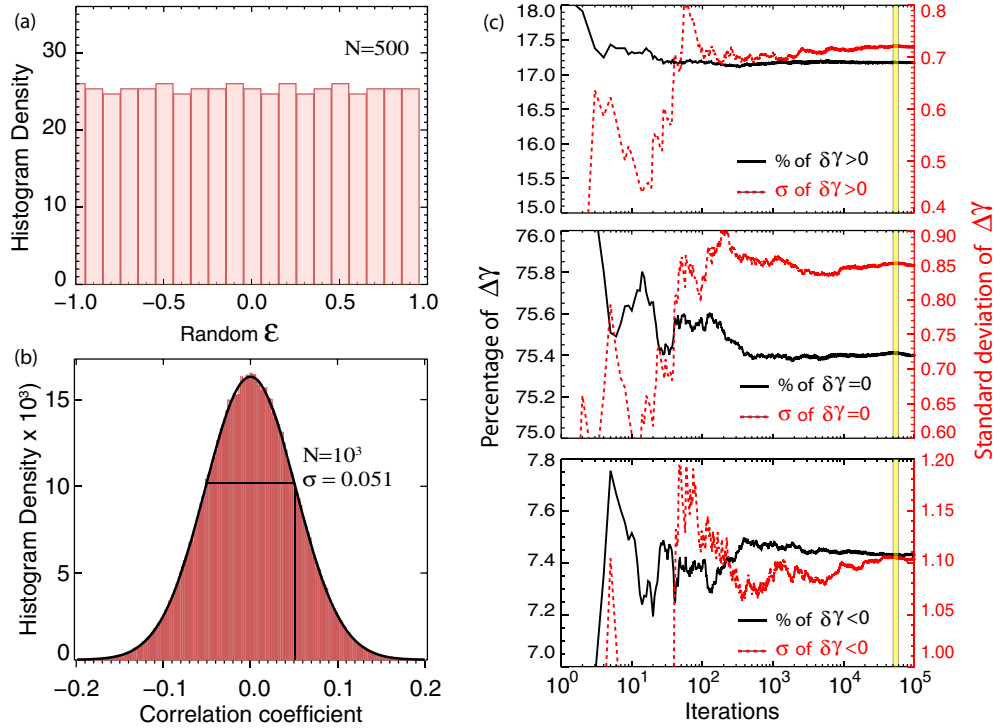
Figure 5. (a) Equidistribution of random numbers $\{\varepsilon_j\}_{j=1}^{385}$ used to randomly imitate the three $\Delta\gamma$ outcomes N_+, N_-, N_0. (b) Histogram of the correlation coefficient between any two sets of random numbers constructed for each iteration, $\{\varepsilon_{i\,j}\}_{j=1}^{385}$, $i = 1, 2, t$. (c) Statistical convergence of the mean and variance of the triplet N_+, N_-, N_0. The iterations are taken up to $t \sim 10^5$, and the final converged values of the means and variances are taken within the yellow shaded interval.
(A color version of this figure is available in the online journal.)

found that ENA emissions in the south and north poles exhibit spectral flattening at high energies but not at lower energies. However, fluxes in all individual channels drop with time at different rates. The flattening at higher energies does not appear to originate from a consistent increase of ENA emissions with increasing energy, but rather from a drop in ENA fluxes at lower energies. If ENA fluxes are correlated with the decrease in the global dynamic pressure (SW density multiplied by the square of the SW speed) measured over the last solar cycle minimum, then the observed spectral trend could be a dispersion effect since high-energy ENAs arrive at *IBEX* faster than low-energy ones. To investigate this, we now compare the observed drop in ENA fluxes over 3 yr with the variation in their SW progenitors during this period. To do so, we first need to trace this parent SW population back in time. Pinning down the source ions of polar ENAs is extremely complex, if not impossible, since both fast and slow SW components exist in the polar HS and these have arrived there along flow streamlines that span across all latitudes. In addition, the slow SW component is much "older" than the fast SW one since it has to travel though much longer deflected streamlines from low and mid-latitudes to high latitudes. Washimi et al. (2011) and Reisenfeld et al. (2012) suggest that finding a direct correlation between HS ENA fluxes with their SW progenitors could indeed be impossible since the HS population is continuously modified by disturbances that originate from variations in the SW dynamic pressure, which in turn affects the termination shock (TS) position, creating pressure pulses that propagate through the HS at the magnetosonic speed. While this scenario is likely, it is not known if the larger timescale (e.g., solar cycle maximum and minimum conditions) would leave an imprint on the globally distributed ENA fluxes. Here, we follow the conventional scenario of tracing back the SW through the streamlines in the HS and

assume that polar ENAs are created from slow or fast SW populations independently to see if a direct correlation with the SW can be inferred.

To calculate the progenitor SW times that would be reasonably linked to the observed ENAs, we need to follow their trajectories back in time. Polar ENAs detected by *IBEX* are generated by ions that traveled along three main routes: (1) SW ions from the Sun to the TS (radial bulk flow), (2) decelerated SW ions from the TS to the ENA conversion point in the HS (curved flow along the streamlines), and (3) ENAs from the SW–ENA conversion point to *IBEX* (radial transport independent of the bulk flow).

Recently, Siewert et al. (2014) provided two-dimensional isochoric transit maps of ENAs based on an analytic model of the parker spiral in the HS (Siewert et al. 2014; see also Fahr & Feitchner 1991). For this analysis, we will use this streamline model and calculate the transit times of ENAs that originate from two different locations in the HS and correspond to slow and fast SW populations. Specifically, (1) ENAs originated from the slow SW component that charge exchanged deep in the polar HS (close to the polar heliopause) along the slow SW streamlines (at 10°, 20°, and 30° from the nose), and (2) ENAs originated in the polar HS region that is closer to the termination shock along the fast SW streamlines (at 60°, 70°, and 80° from the nose). Figure 6(a) illustrates this geometry. We note that this streamline model is centered around the nose, while *IBEX* data is acquired in a slightly shifted frame of reference (nose is at $-4.98° \pm 0.21°$ ecliptic J2000 latitude; McComas et al. 2012a). However, we did not account for this for the sake of simplicity and eye guidance.

We now track the SW particles as they travel out from the Sun. As a first-order approximation and consistent with in situ observations, the SW decelerates gradually as it travels
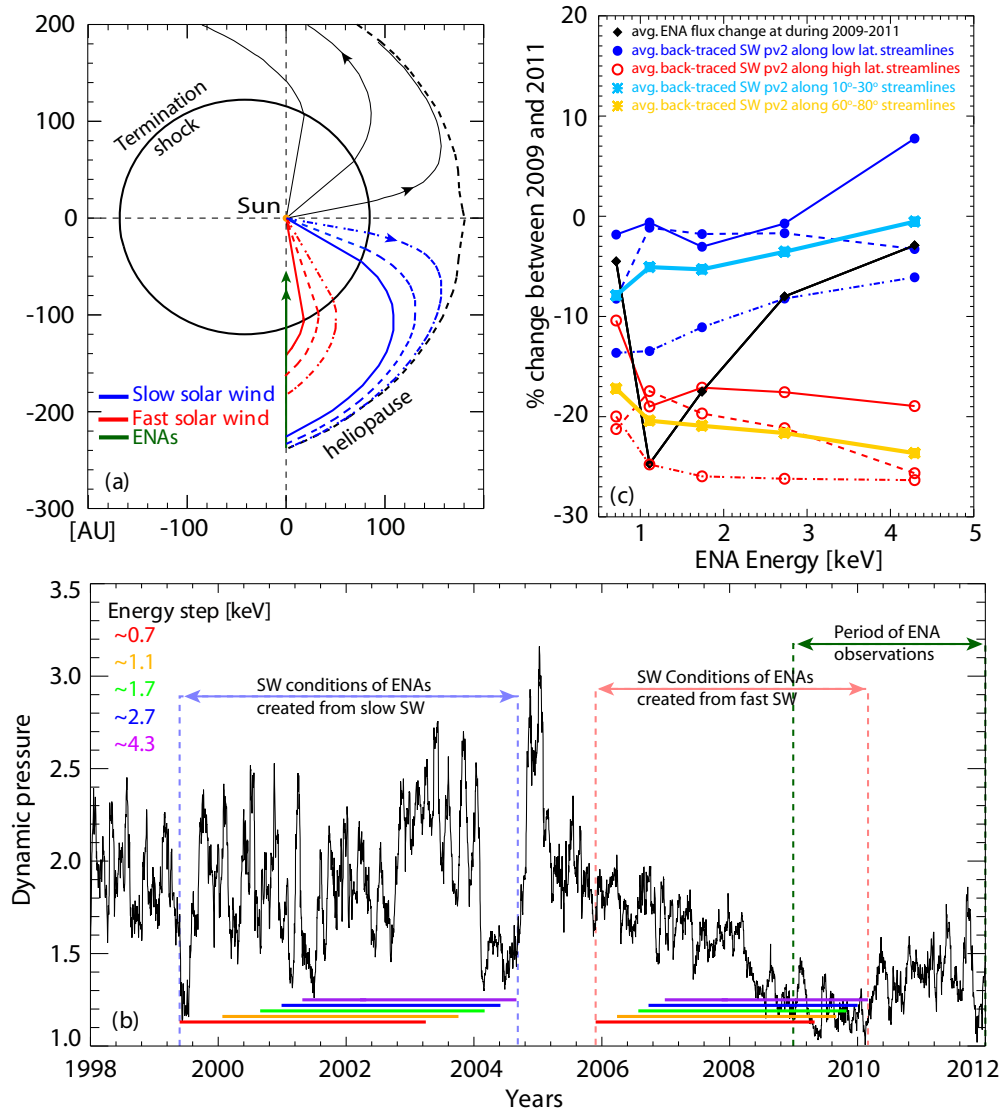
Figure 6. (a) Schematic side view of the heliosphere illustrating the streamlines along which the fast SW from high latitudes (red; >60°), and the slow SW from mid- and low latitudes (blue; <30°), ENAs are assumed to be created via charge exchange in the poles in the HS (green arrows). (b) SW dynamic pressure measured at 1 AU. Colored horizontal lines indicate the time periods corresponding to the SW conditions at the time where ENAs observed between 2009 and 2011 are created, assuming both slow and fast SW source origins in the polar HS. (c) Percentage change of south pole averaged ENA fluxes (black) and averaged SW dynamic pressure obtained during the corresponding time periods in panel (b), assuming mixed slow and fast SW populations. Line styles (solid, dashed, and dash–dotted) correspond to the different streamlines in panel (a). Sky blue and orange lines represent the averaged values corresponding to low (blue) and high (red) latitude streamlines, respectively.

(A color version of this figure is available in the online journal.)

radially from the Sun because of the mass loading of SW due to charge exchange between the interstellar neutral hydrogen atoms and SW protons by ~10% (e.g., Schwadron et al. 2011; Siewert et al. 2014; Richardson 2008). As it crosses the TS, the SW is decelerated again by almost a factor of two. It is not known how the downstream SW bulk speed in the HS varies at different latitudes (except through models; see, for example, Fahr et al. 2000), but we will consider it fixed for simplicity. When the SW reaches the poles, ions undergo charge exchange and create an ENA that travels back inward to *IBEX*, located at 1 AU, unhindered by the electromagnetic forces. Under these assumptions, the total transit time of an ENA observed by *IBEX* at the poles is

$$t = \frac{d_{\mathrm{TS}o}}{v_{\mathrm{sw}}} + \frac{S}{v_s} + \frac{d_{\mathrm{TS}i} + D_{\mathrm{HS}}}{v_{\mathrm{ENA}}}, \quad (1)$$

where $d_{\mathrm{TS}o}$ and $d_{\mathrm{TS}i}$ are the distances from the Sun to the TS outbound (path where SW is going away from the Sun) and inbound (ENAs crossing the distance from the TS toward *IBEX*), v_{sw} is the SW speed, S is the length of the curved streamline from the TS to the point of SW–ENA conversion, v_s is the downstream speed of the SW ions, D_{HS} is the HS thickness at the point of SW–ENA conversion, and v_{ENA} is the ENA speed. Note that S, D_{HS}, d_{TS}, and v_s are model dependent, with S being more complex as it is almost impossible to predict.

The first two terms in Equation (1) describe the travel time of the SW ion from the Sun to the SW–ENA conversion point, and the third term represents the time for the ENAs to travel back to *IBEX*. The averaged arc lengths of the slow and fast SW streamlines of Figure 6(a) are ~378 AU (between 10° and 30° relative to the nose) and ~185 AU (between 60° and 80° relative to the nose), respectively. We also assume an averaged

Table 4
Transit Times of Outgoing SW and Coming ENAs Through the Paths Illustrated in Figure 6

E Step	E_{-HM}[a]	E_{nom}[a]	E_{+HM}[a]	Travel Times Based on a Slow SW Source along a Streamline Originating at a Specific Latitude (yr)			Travel Times Based on a Fast SW Source along a Streamline Originating at a Specific Latitude (yr)		
				10°	20°	30°	60°	70°	80°
2	0.52	~0.7	0.95	12.8–13.7	11.3–12.2	10.1–10.9	4.2–4.9	3.5–4.2	2.8–3.3
3	0.84	~1.1	1.55	12.2–13.0	10.7–11.4	9.5–10.2	3.8–4.4	3.2–3.7	2.4–2.9
4	1.36	~1.7	2.50	11.7–12.3	10.3–10.9	9.1–9.6	3.4–3.9	2.9–3.2	2.2–2.5
5	1.99	~2.7	3.75	11.4–11.9	9.9–10.5	8.8–9.3	3.2–3.6	2.6–2.9	2.0–2.3
6	3.13	~4.3	6.00	11.2–11.6	9.7–10.1	8.5–8.9	3.0–3.3	2.5–2.7	1.8–2.1

Note. [a] Funsten et al. (2009a).

slow SW speed of ~392 km s^{-1} (~0.8 keV) and a fast SW speed of ~760 km s^{-1} (~3.0 keV; Ebert et al. 2009).

Substituting these values in Equation (1), we find that it takes ~11.1 yr and ~3.4 yr, respectively, for a ~1.1 keV ion that originates at 20° and 70° from the Sun to travel through the heliosphere to the TS, then through the HS along the streamlines, and finally charge exchange and come back to 1 AU. Table 4 lists the ENA transit times for all energies and along both slow and fast SW paths illustrated in Figure 6. Results are consistent with those from a recent study performed by Siewert et al. (2014).

Using these results, we now infer the conditions back in time when the SW progenitors of the observed ENAs were created (maintaining the slow and fast SW source assumptions). This will be in the context of the dynamic pressure since it best describes the SW conditions in the heliosphere. First, it balances the external pressure from the local interstellar medium and thus contributes in controlling the size of the heliosphere. Second, it is an excellent indicator of the solar energy output, which is mostly carried by the SW bulk flow (McComas et al. 2008). In addition, *Ulysses* observations suggest that the global variations in this quantity are independent of latitude (e.g., Richardson & Wang 1999; McComas et al. 2008).

Figure 6(b) shows the dynamic pressure variations between 1998 and 2012 at 1 AU. Color-coded dashes mark the time periods corresponding to the SW conditions at the time where ENAs observed between 2009 and 2011 are created, assuming both slow and fast SW are possible source origins of ENAs in the polar HS. We then calculate the averaged dynamic pressure during each of these time periods and compare them to the observed *IBEX*'s polar ENA variations. This is shown in Figure 6(c).

Figure 6(c) shows that variations in ENA fluxes between 2009 and 2011 at all energies do not appear to consistently correlate with the averaged dynamic pressure of the back-traced SW population at the HS polar regions. If anything, the averaged slow SW component (light blue) is probably positively correlated with the ENA variations while the averaged fast SW component is negatively correlated (orange).

The lack of a significant and consistent correlation between ENAs and the SW by back-tracing the progenitor SW along the flow streamlines becomes understandable considering the different sources that affect this correlation. (1) For instance, the length of the streamlines is directly related to the back-traced times of the SW and thus selecting a specific stream line at a certain latitude would directly affect the correlation. (2) Polar ENAs observed at 1 AU come from a line of sight that cuts through a set of streamlines whose origins span

all latitudes; the assumption here that they are created from a specific (slow or fast) population is not necessarily valid. (3) Flow streamlines in the HS are constantly modified due to solar transients and the global solar output; it is possible that by the time the SW population reaches the poles via the streamlines, their distribution could be modified so that particles have different thermal properties. (4) The model we used assumes full symmetry between the north and south with the heliospheric streamlines divergence point (nose) being in the middle. (5) The structure of the SW in the HS at different latitudes is not known, and it is likely that the assumption of a fixed speed may not be valid. (6) The SW dynamic pressure fluctuates dramatically at short timescales (days) compared with the inferred SW back-traced times (years), hence making a quantitative relation with ENAs over short timescales unrealistic. (7) Finally, without further acceleration, ENAs originating from slow and fast SW in the HS correspond to energies of ~1 keV and ~3 keV, respectively. Hence, ENAs at ~4.3 keV must have been accelerated by some mechanism(s) and at some location(s) along the line of sight, which are yet to be understood. This work assumes that ENAs at ~2.7 and ~4.3 keV come from the fast SW component.

Considering all these reasons, the SW could still have a much longer-timescale (years) effect on ENA production that is not observable over short periods of time. The persistent large and global short-term fluctuations of the SW dynamic pressure on short timescales could, in principle, leave a print on the HS populations by consistently adjusting the heliosphere and resulting in continuous ram pressure pulses that constantly change the position of the TS, hence creating magnetosonic pulses downstream in the HS and modifying the SW populations. This scenario was further investigated with MHD simulations recently performed by Washimi et al. (2011), highlighting the ram-pressure effect on the HS plasmas.

In Figure 6(b), during the time period of inferred SW conditions for ENAs created from a slow SW population (1999.6–2004.3), the SW dynamic pressure fluctuated by more than a factor of two over reasonably short time periods (months). On the other hand, it fluctuated much less over similar timescales during the back-traced times for the fast SW (~2006–2010). While this could be related to the slight correlation of ENA fluxes with the averaged SW dynamic pressure from low (10°–30°) and high (60°–80°) latitudes, it is not clear how this directly affects ENA production in that region.

In summary, we examined ENA flux variations at the heliospheric polar regions at energies between ~0.7 keV and ~4.3 keV. We found an overall flattening of the ENA spectra in the north and south polar regions at energies above

~1.7 keV. This flattening is caused by a drop in ENA fluxes at lower energies. This drop increases with decreasing energy. In addition, we did not find a clear correlation between the observed ENA flux variations during the 2009–2011 period and their respective progenitors in the slow and fast SW component coming from low and high latitudes, back-traced along the flow streamlines. These results shed light on the complexity of identifying the sources of variations in ENA globally distributed fluxes, in particular at the polar regions. Relating ENA fluxes with their SW progenitors is complex and these results further highlight the need for modern three-dimensional MHD/kinetic models, which incorporates realistic and time-varying heliospheric models.

REFERENCES

Allegrini, F., Bzowski, M., Dayeh, M. A., et al. 2012, ApJL, 749, 41
Bame, S. J., McComas, D. J., Barraclough, B. L., et al. 1992, A&AS, 92, 237
Dayeh, M. A., McComas, D. J., Allegrini, F., et al. 2012, ApJ, 749, 50
Dayeh, M. A., McComas, D. J., Livadiotis, G., et al. 2011, ApJ, 734, 29
Ebert, R. W., McComas, D. J., Elliott, H. A., Forsyth, R. J., & Gosling, J. T. 2009, JGR, 114, 01109
Fahr, H.-J., & Fichtner, H. 1991, SSRv, 58, 193
Fahr, H. J., Kausch, T., & Scherer, H. 2000, A&A, 357, 268
Funsten, H. O., Allegrini, F., Bochsler, P., et al. 2009a, SSRv, 146, 75
Funsten, H. O., Allegrini, F., Crew, G. B., et al. 2009b, Sci, 326, 964
Funsten, H. O., Demajistre, R., Frisch, P. C., et al. 2013, ApJ, 776, 30
Fuselier, S. A., Bochsler, P., Chornay, D., et al. 2009, SSRv, 146, 117
Livadiotis, G. 2007, PhyA, 375, 518
Livadiotis, G. 2014, J. Stat. Distr. Appl., 1, 4
Livadiotis, G., McComas, D. J., Dayeh, M. A., Funsten, H. O., & Schwadron, N. A. 2011, ApJ, 734, 1
Livadiotis, G., McComas, D. J., Randol, B. M., et al. 2012, ApJ, 751, 64
McComas, D. J., Alexashov, D., Bzowski, M., et al. 2012a, Sci, 336, 1291
McComas, D. J., Allegrini, F., Bochsler, P., et al. 2009, SSRv, 146, 11
McComas, D. J., Bzowski, M., Frisch, P., et al. 2010, JGR, 115, 09113
McComas, D. J., Dayeh, M. A., Allegrini, F., et al. 2012b, ApJS, 203, 1
McComas, D. J., Dayeh, M. A., Funsten, H. O., Livadiotis, G., & Schwadron, N. A. 2013, ApJ, 771, 77
McComas, D. J., Ebert, R. W., Elliott, H. A., et al. 2008, GeoRL, 35, 18103
McComas, D. J., Funsten, H. O., Fuselier, S. A., et al. 2011, GeoRL, 38, L18101
McComas, D. J., Riley, P., Gosling, J. T., Balogh, A., & Forsyth, R. 1998, JGR, 103, 1955
Reisenfeld, D. B., Allegrini, F., Bzowski, M., et al. 2012, ApJ, 747, 110
Richardson, J. D., Kasper, J. C., Wang, C., Belcher, J. W., & Lazarus, A. J. 2008, Natur, 454, 63
Richardson, J., & Wang, C. 1999, GeoRL, 26, 561
Schwadron, N. A., Allegrini, F., Bzowski, M., et al. 2011, ApJ, 731, 56
Siewert, M., Fahr, H.-J., & McComas, D. J. 2014, A&A, 565, A81
Washimi, H., Zank, G. P., Hu, Q., et al. 2011, MNRAS, 416, 1475